DEFENCE RESEARCH AGENCY
MALVERN

MEMORANDUM No. 4577

ISAR IMAGING OF MARITIME TARGETS: THEORY AND SIMULATION

Authors: N J Porter, R J A Tough & K D Ward

DEFENCE RESEARCH AGENCY,
MALVERN,
WORCS.

MEMORANDUM No. 4577

UNLIMITED

DEFENCE RESEARCH AGENCY
MALVERN

MEMORANDUM No. 4577

ISAR IMAGING OF MARITIME TARGETS: THEORY AND SIMULATION

N J Porter, R J A Tough and K D Ward

Date: September 1992

SUMMARY

The theoretical analysis of synthetic aperture techniques presented in Memorandum 4532 is applied to the inverse synthetic aperture radar (ISAR) imaging of ship targets. The point spread function of an ISAR system is derived and discussed in detail. The explicit representation of phase information within our formalism makes possible the first thorough analysis of interference effects in synthetic aperture images of closely spaced scatterers. Effects of errors in motion compensation are also discussed in considerably greater depth than in earlier work. Computer simulation has provided us with a useful tool with which to verify our analytical results; we describe our simulation method and present a comprehensive selection of simulated images illustrating and confirming our theoretical analysis. Finally some practical implications of our results for the autofocusing of ISAR images are discussed.

This work was carried out under Defence Research Package AS02BM23

Contents

1 Introduction

In a recent memorandum [1] we described a unified theory of SAR,ISAR and hybrid SAR/ISAR imaging of targets which took account of target rotational motions and the relative centre of mass motions of the target and the radar platform. Some preliminary simulations of the ISAR imaging of a point target were also presented and were found to be in excellent agreement with the predictions of our formal analysis.

In this paper we will discuss the implications of this work for ISAR imaging in considerable detail. After reviewing the basic concepts and formalism of [1] we apply these methods to analyse the principles of ISAR more clearly and in much greater depth than has been done in pevious work. Particular attention is paid to the properties of the complex (I,Q), rather than the real, intensity, image so that we are able to describe coherent interference effects in images of closely spaced scatterers for the first time. Image degradation due to errors in motion compensation is also discussed exhaustively. In both these cases the powerful techniques introduced in [1] once again provide us with a concise, physically transparent description of effects which would be prohibitively difficult to analyse within the context of standard ISAR theory.

Computer simulation provides us with a useful tool with which to confirm our theoretical findings. Consequently we describe our methodology in more detail than was done in [1] and present an extensive set of simulated images demonstrating, and confirming in detail, our theoretical results. Finally we discuss the practical implications of our findings for the autofocusing of ISAR images.

2 The k-space description of synthetic aperture imaging

In our earlier work [1] we presented a general theoretical framework within which we can describe synthetic aperture imaging concisely and in detail. The application of these methods to the special case of inverse synthetic aperture radar (ISAR) is discussed in this section, permitting us to simplify and clarify several features of our original approach. Our initial discussion also serves to make the present work essentially self contained, by providing background material for our subsequent discussions of interference effects and the defocusing and distortion of images arising from errors in motion compensation and allowing us to discuss our detailed simulation studies in the overall context of the k-space formalism.

2.1 Evaluation of the Point Spread Function

An appealing feature of the k-space formalism we apply to the imaging process is the way in which its component parts correspond directly to operations carried out in the process itself. Thus in the case of ISAR a signal propagates at time t with wavenumber $\frac{k}{2}$ (the factor of $\frac{1}{2}$ is included for subsequent convenience) from a source at a distance $r(t)$ along a line of sight vector $\hat{\mathbf{r}}$ to a point target at $\mathbf{r}'(t)$, whose motion is due to its rotation about the origin of our coordinate system. In a monostatic configuration the signal propagates back to $r(t)\hat{\mathbf{r}}$ and is received as

$$S_1(k,t) = \exp(ik|r(t)\hat{\mathbf{r}} - \mathbf{r}'(t)|) \tag{1}$$

The rotational motion of $\mathbf{r}'(t)$ can be represented by

$$\mathbf{r}'(t) = \mathbf{M}_s(t).\mathbf{r}' \tag{2}$$

where $\mathbf{r}'$ is the position of the imaged point at time zero. $\mathbf{M}_s(t)$ is the linear operator generating the target rotation in time t [1,2]. As this is orthogonal we have

$$|r(t)\hat{\mathbf{r}} - \mathbf{r}'(t)| = |\mathbf{r}(t) - \mathbf{r}'| \tag{3}$$

where

$$\mathbf{r}(t) = r(t)\mathbf{M}_s^{-1}(t).\hat{\mathbf{r}} \tag{4}$$

Thus we may write

$$S_1(k,t) = \exp(ik|\mathbf{r}(t) - \mathbf{r}'|). \tag{5}$$

(The return from an extended target may be derived by integrating $\mathbf{r}'$ over the spatial extent of the target, with a suitable scattering function weighting [1].) Knowing the range $r(t)$ we can subject this signal to motion compensation to give

$$S_2(k,t) = \exp(-ikr(t) + ik|\mathbf{r}(t) - \mathbf{r}'|) \tag{6}$$

If, as in [1], we consider imaging in the far field, we may approximate this by

$$S_2(k,t) = \exp(-i\mathbf{k}(t).\mathbf{r}') \tag{7}$$

where $\mathbf{k}(t) = k\mathbf{M}_s^{-1}(t).\hat{\mathbf{r}}$, so that returns at successive times t provide a set of spatial Fourier components of the point target's position at time zero, with wave vectors selected by its own rotational motion and by the frequency modulation applied to the transmitted waveform. Thus, if the rotation of the target is specified by an axis $\mathbf{n}_s$ and an angular velocity ω [1,2] we have

$$\mathbf{k}(t) = (k_0 + \delta k)\left((1 - \cos(\omega t))\mathbf{n}\mathbf{n}.\hat{\mathbf{r}} + \cos(\omega t)\hat{\mathbf{r}} + \sin(\omega t)(\mathbf{n} \wedge \hat{\mathbf{r}})\right). \tag{8}$$

Here

$$k_0 = \frac{4\pi f_0}{c}$$

where f_0 is the centre transmitted frequency and c is the velocity of light, δk is the change in transmitted wave number due to frequency modulation and $\mathbf{n} = -\mathbf{n}_s$ (c.f. (4)). On expanding (8) to second order in δk and ωt we find that

$$\mathbf{k}(t) = k_0\hat{\mathbf{r}} + k_0\omega t\mathbf{n}\wedge\hat{\mathbf{r}} + \delta k\omega t\mathbf{n}\wedge\hat{\mathbf{r}} + \frac{k_0}{2}\omega^2t^2\mathbf{n}\wedge(\mathbf{n}\wedge\hat{\mathbf{r}}) \tag{9}$$

Consequently k space is interrogated on the surface of a cone with axis $\mathbf{n}$ and containing $\mathbf{k}_0$ [1]. In [1] we showed that conventional ISAR processing is equivalent to the Fourier inversion of these components, assuming them to be sampled uniformly on a Cartesian grid whose 1,2 axes $(\hat{\mathbf{e}}_1, \hat{\mathbf{e}}_2)$ are parallel to $\hat{\mathbf{r}}, \mathbf{n}\wedge\hat{\mathbf{r}}$ respectively. (This coordinate sytem, supplemented by a third orthogonal axis $\hat{\mathbf{e}}_3$ parallel to $\hat{\mathbf{r}}\wedge(\mathbf{n}\wedge\hat{\mathbf{r}})$ will be adopted throughout our subsequent discussion.) We now make the following identifications:

$$\mathbf{k}_0 = k_0\hat{\mathbf{r}} \tag{10}$$

$$\mathbf{k}_{H1} = \delta k\hat{\mathbf{r}} = k_{H1}\frac{\mathbf{k}_0}{k_0} \tag{11}$$

$$\mathbf{k}_{H2} = \omega_s t\mathbf{n}\wedge\mathbf{k}_0 = k_{H2}\frac{\mathbf{n}\wedge\mathbf{k}_0}{k_0|\sin\Omega|} \tag{12}$$

where Ω is the angle between $\mathbf{n}, \mathbf{k}_0$. One dimensional Fourier inversion with respect to k_{H1} is equivalent to the acquisition of range resolution by pulse compression while subsequent inversion with respect to k_{H2} is equivalent to the Doppler component of ISAR processing. δk and t may be eliminated from the remaining terms in (9) to give

$$\mathbf{k}(t) = \mathbf{k}_0 + \mathbf{k}_H + \delta\mathbf{k}(\mathbf{k}_H) \tag{13}$$

where

$$\delta\mathbf{k}(\mathbf{k}_H) = k_{H1}\frac{\mathbf{k}_{H2}}{k_0} + \frac{1}{2}\frac{\omega_s^2k_{H2}^2}{k_0\sin^2\Omega}\mathbf{n}\wedge(\mathbf{n}\wedge\hat{\mathbf{r}}) \tag{14}$$

$$= \frac{k_{H1}k_{H2}}{k_0}\hat{\mathbf{e}}_2 + \frac{1}{2}\frac{\omega_s^2k_{H2}^2}{k_0\sin^2\Omega}\left(\cos\Omega\sin\Omega\hat{\mathbf{e}}_3 - \sin^2\Omega\hat{\mathbf{e}}_1\right) \tag{15}$$

(This straightforward analysis yields the result expressed in [1] as

$$\delta k_\alpha = \frac{1}{2}C_{\alpha\beta\gamma}k_{H\alpha}k_{H\gamma},$$

and allows us to identify elements of the curvature tensor $C_{\alpha\beta\gamma}$ immediately. Here and elsewhere we adopt the convention of summation over repeated indices.)

By bringing these results together we may write the point spread function of the ISAR system as

$$H(\mathbf{r}_H, \mathbf{r}') = \frac{e^{i\mathbf{k}_o\cdot(\mathbf{r}_H-\mathbf{r}'_H)}}{(2\pi)^2}\int d^2k_H e^{i\mathbf{k}_H\cdot(\mathbf{r}_H-\mathbf{r}'_H)-i\mathbf{r}'\cdot\delta\mathbf{k}}\tilde{H}(\mathbf{k}_H) \tag{16}$$

$\tilde{H}(\mathbf{k}_H)$ is the weighting in k-space resulting from the system's beam and bandwidth and is modelled conveniently by the Gaussian function

$$\tilde{H}(\mathbf{k}_H) = \frac{\exp\left(-\frac{1}{2}\tilde{\mathbf{k}}_H.\mathbf{D}.\mathbf{k}_H\right)}{(2\pi)(\det\mathbf{D}^{-1})^{\frac{1}{2}}} \tag{17}$$

where

$$\mathbf{D} = \begin{pmatrix} d_{11} & 0 \\ 0 & d_{22} \end{pmatrix}$$

The phase term $\exp(-i\mathbf{r}'.\delta\mathbf{k})$ can be expressed similarly as $\exp\left(-\frac{i}{2}\tilde{\mathbf{k}}_H.\mathbf{C}.\mathbf{k}_H\right)$ where

$$\mathbf{C} = \begin{pmatrix} c_{11} & c_{12} \\ c_{21} & c_{22} \end{pmatrix} \tag{18}$$

with $c_{\beta\gamma} = r'_\alpha C_{\alpha\beta\gamma} = c_{\gamma\beta}$ or, more explicitly

$$\mathbf{C} = \begin{pmatrix} 0 & \frac{r'_2}{k_0} \\ \frac{r'_2}{k_0} & -\frac{(r'_1 - r'_3\cot\Omega)}{k_0} \end{pmatrix} \tag{19}$$

Thus we may express the point spread function in the form

$$H(\mathbf{r}_H, \mathbf{r}') = \frac{e^{i\mathbf{k}_o.(\mathbf{r}_H - \mathbf{r}'_H)}}{(2\pi)^3(\det\mathbf{D}^{-1})^{\frac{1}{2}}} \int d^2\mathbf{k}_H e^{i\mathbf{k}_H.(\mathbf{r}_H - \mathbf{r}'_H)} \exp\left(-\frac{1}{2}\tilde{\mathbf{k}}_H.(\mathbf{D} + i\mathbf{C}).\mathbf{k}_H\right) \tag{20}$$

$$= \frac{e^{i\mathbf{k}_0.\Delta\mathbf{r}_H}}{(2\pi)^2(\det\mathbf{D}^{-1})^{\frac{1}{2}})} \frac{2\pi}{[(\alpha-\beta)^2+\gamma^2]^{\frac{1}{4}}} \exp\left(-\frac{i}{2}\tan^{-1}\left[\frac{\gamma}{\alpha-\beta}\right]\right)$$

$$\times \exp\left(-\frac{1}{2}\Delta\tilde{\mathbf{r}}_H.\mathbf{A}.\Delta\mathbf{r}_H\right) \exp\left(-\frac{i}{2}\Delta\tilde{\mathbf{r}}_H.\mathbf{P}.\Delta\mathbf{r}_H\right) \tag{21}$$

where $\alpha = d_{11}d_{22}$, $\beta = c_{11}c_{22} - c_{12}^2$, $\gamma = d_{11}c_{22} + d_{22}c_{11}$ and $\Delta\mathbf{r}_H = \mathbf{r}_H - \mathbf{r}'_H$,

$$\mathbf{A} = \frac{(\alpha-\beta)\mathrm{Adj}\mathbf{D} + \gamma\mathrm{Adj}\mathbf{C}}{(\alpha-\beta)^2+\gamma^2}$$

$$= \begin{pmatrix} \frac{(\alpha-\beta)d_{22}+\gamma c_{22}}{(\alpha-\beta)^2+\gamma^2} & \frac{-\gamma c_{21}}{(\alpha-\beta)^2+\gamma^2} \\ \frac{-\gamma c_{12}}{(\alpha-\beta)^2+\gamma^2} & \frac{(\alpha-\beta)d_{11}+\gamma c_{11}}{(\alpha-\beta)^2+\gamma^2} \end{pmatrix} \tag{22}$$

and

$$\mathbf{P} = \frac{(\alpha-\beta)\mathrm{AdjC} + \gamma\mathrm{AdjD}}{(\alpha-\beta)^2+\gamma^2}$$

$$= \begin{pmatrix} \frac{(\alpha-\beta)c_{22}-\gamma d_{22}}{(\alpha-\beta)^2+\gamma^2} & \frac{-(\alpha-\beta)c_{21}}{(\alpha-\beta)^2+\gamma^2} \\ \frac{-(\alpha-\beta)c_{12}}{(\alpha-\beta)^2+\gamma^2} & \frac{(\alpha-\beta)c_{11}-\gamma d_{11}}{(\alpha-\beta)^2+\gamma^2} \end{pmatrix}. \tag{23}$$

The amplitude variation within the point spread function is contained in the Gaussian function $\exp\left(-\frac{1}{2}\Delta\tilde{\mathbf{r}}_H.\mathbf{A}.\Delta\mathbf{r}_H\right)$ while the phase variation is contained in the term $\exp\left(-\frac{i}{2}\Delta\tilde{\mathbf{r}}_H.\mathbf{P}.\Delta\mathbf{r}_H\right)$. In [1] we have shown how the lower order moments of the point spread function are related simply to the elements of **C** and **D** through

$$\langle(\Delta x)^2\rangle = d_{11} + \frac{c_{11}^2}{d_{22}} \tag{24}$$

$$\langle\Delta x\Delta y\rangle = \frac{c_{12}c_{22}}{d_{11}} \tag{25}$$

and

$$\langle(\Delta y)^2\rangle = d_{22} + \frac{c_{22}^2}{d_{22}} + \frac{c_{12}^2}{d_{11}} \tag{26}$$

The confirmation of these results by computer simulation is presented in [1]. The compact representation of the phase variation within the point spread function enables us to describe interference effects within synthetic aperture images of closely spaced scatterers by the appropriate coherent summation of point spread functions centred on the positions of the scatterers. The amplitude and phase of the resulting function will then characterise the detailed structure of the corresponding ISAR image. This procedure will be illustrated by computer simulation in a subsequent section of this Memorandum.

2.2 Motion Compensation Errors

The **C** matrix formalism we have just described is sufficiently flexible to accommodate defocusing effects due to errors in motion compensation i.e. in the estimation of the position of the centre of rotation of the target. A preliminary discussion of this general problem was given in [1]; by restricting our present discussion to inverse synthetic aperture radar we are able to highlight several points which were neglected in our earlier work. Once again our formalism has become more streamlined so that much of the algebraic drudgery that was evident in [1] can be avoided.

Let us assume that we have made an error $\delta\mathbf{r}(t)$ in estimating the position of the centre of rotation of the target. The returned signal $S_1(k,t)$ is now given by

$$S_1(k,t) = \exp(ik|r(t)\hat{\mathbf{r}} - \mathbf{M}_s(t).\mathbf{r}' - \delta\mathbf{r}(t)|). \tag{27}$$

which, when subjected to motion compensation based on the range estimate $r(t)$ yields (in the far field limit)

$$S_2(k,t) = \exp(-i\mathbf{k}(t).\mathbf{r}' - i\mathbf{k}(t).\mathbf{M}_s^{-1}(t).\delta\mathbf{r}(t)) \tag{28}$$

Thus we see how the phase of the processed signal has been altered as a result of incorrect motion compensation. This phase change results in a shift in the position of the centre of the point spread function, which is also subject to a further defocusing. Quantitative measures of these effects can be obtained by expanding this phase change to $O(k_H^2)$; the linear term will specify the image shift while the quadratic terms characterise the extra defocusing and may be represented concisely by a suitable augmentation of the elements of the **C** matrix (19). As before we write

$$\mathbf{k}(t) = (1 + \frac{k_{H1}}{k_0})\left(\mathbf{k_0} + \omega t(\mathbf{n} \wedge \mathbf{k}_o) + \frac{\omega^2 t^2}{2}\mathbf{n} \wedge (\mathbf{n} \wedge \mathbf{k_0})\right). \tag{29}$$

If $\delta\mathbf{r}(t)$ is expressed in terms of a gross displacement error $\bar{\delta\mathbf{r}}$, a velocity **v** and an acceleration **a** through

$$\delta\mathbf{r}(t) = \bar{\delta\mathbf{r}} + \mathbf{v}t + \frac{1}{2}\mathbf{a}t^2 \tag{30}$$

we find by direct expansion that

$$\mathbf{M}_s^{-1}(t).\delta\mathbf{r}(t) = \bar{\delta\mathbf{r}} + (\mathbf{v} + \mathbf{n} \wedge \bar{\delta\mathbf{r}})t + \frac{1}{2}(\mathbf{a} + 2\omega\mathbf{n} \wedge \mathbf{v} + \omega^2\mathbf{n} \wedge (\mathbf{n} \wedge \bar{\delta\mathbf{r}}))t^2 \tag{31}$$

where **v** and **a** have been supplemented by terms corresponding to the centrifugal and Coriolis corrections applied in the discussion of dynamics referred to a rotating coordinate frame[3]. By expanding

$$\mathbf{k}(t).\mathbf{M}_s^{-1}(t).\delta\mathbf{r}(t) = (1 + \frac{k_{H1}}{k_0})\left(\mathbf{k_0} + \omega t(\mathbf{n} \wedge \mathbf{k_0}) + \frac{\omega^2 t^2}{2}\mathbf{n} \wedge (\mathbf{n} \wedge \mathbf{k_0})\right)$$

$$.\left(\bar{\delta\mathbf{r}} + (\mathbf{v} + \mathbf{n} \wedge \delta\mathbf{r})t + \frac{1}{2}(\mathbf{a} + 2\omega\mathbf{n} \wedge \mathbf{v} + \omega^2\mathbf{n} \wedge (\mathbf{n} \wedge \bar{\delta\mathbf{r}}))t^2\right), \tag{32}$$

exploiting the vector identities

$$(\mathbf{n} \wedge (\mathbf{n} \wedge \mathbf{k_0}).\bar{\delta\mathbf{r}}) = (\mathbf{n} \wedge (\mathbf{n} \wedge \bar{\delta\mathbf{r}}).\mathbf{k_0} = -(\mathbf{n} \wedge \mathbf{k_0}).(\mathbf{n} \wedge \bar{\delta\mathbf{r}})$$

and eliminating t (c.f. (12)) we find that

$$\mathbf{k}(t).\mathbf{M}_s^{-1}(t).\delta\mathbf{r}(t) = \mathbf{k}_0.\bar{\delta}\mathbf{r} + k_{H1}\bar{\delta r}_{H1}$$

$$+ \frac{\mathbf{k}_0.\mathbf{v}k_{H2}}{\omega|\mathbf{n}\wedge\mathbf{k}_0|} + \frac{(\mathbf{k}_0.\mathbf{v})k_{H1}k_{H2}}{k_0\omega|\mathbf{n}\wedge\mathbf{k}_0|} + \frac{1}{2}\frac{\mathbf{k}_0.\mathbf{a}k_{H2}^2}{\omega^2|\mathbf{n}\wedge\mathbf{k}_0|^2}, \tag{33}$$

noting the exact cancellation of terms arising from the centrifugal and Coriolis corrections. The point spread function incorporating the effects of errors in motion compensation is given by

$$H(\mathbf{r}_H,\mathbf{r}') = \frac{1}{(2\pi)^2}e^{i\mathbf{k}_0.(\mathbf{r}_H-\mathbf{r}')}\int d^2k_H e^{i(\mathbf{k}_H.\mathbf{r}_H-\mathbf{k}.(\mathbf{r}'+\mathbf{M}_s(t)^{-1}.\delta\mathbf{r}(t))}H(\tilde{\mathbf{k}}_H) \tag{34}$$

On comparing this result with (16) we see that the presence of the zeroth order term in (33) merely multiplies the point spread function by a constant phase factor $\exp(-i\mathbf{k}_0.\bar{\delta}\mathbf{r})$. The linear term in (33) shifts the centre of the point spread function from

$$\mathbf{r}_H = \mathbf{r}'_H$$

to

$$\mathbf{r}_H = \mathbf{r}'_H + \delta r_{H1}\hat{\mathbf{e}}_1 + \frac{v_1}{\omega|\sin\Omega|}\hat{\mathbf{e}}_2$$

while the quadratic terms modify the defocusing to that represented by the C matrix

$$\mathbf{C} = \begin{pmatrix} 0 & \frac{1}{k_0}\left(r'_2 + \frac{v_1}{\omega|\sin\Omega|}\right) \\ \frac{1}{k_0}\left(r'_2 + \frac{v_1}{\omega|\sin\Omega|}\right) & -\frac{1}{k_0}\left(r'_1 - r'_3\cot\Omega - \frac{a_1}{\omega^2\sin^2\Omega}\right) \end{pmatrix} \tag{35}$$

Thus we see that the position of the image is shifted by the along range part of the gross error in the estimation of the target/platform separation, and across the line of sight by the uncompensated along range velocity. This observation is consistent with the ISAR technique acquiring across range resolution only through the rotational motion of the target and so being incapable of detecting the constant $\bar{\delta r}_2$. We also note that the modified C matrix (35) is independent of $\bar{\delta}\mathbf{r}$. This is a physically reasonable result as we can see by considering the special case of a point target at the origin of the coordinate system. Merely misplacing such a target (which is not affected by rotation) cannot cause defocusing; our inclusion of centrifugal and Coriolis type terms in the analysis has eliminated the dependence of C on $\bar{\delta}\mathbf{r}$ and so has ensured that our formal and intuitive understandings of the imaging process are in accord.

From (24-26) we see that the lower order moments of the point spread function, corrupted by incorrect motion compensation, are given by

$$\langle(\Delta x)^2\rangle = d_{11} + \frac{1}{d_{22}k_0^2}\left(\frac{r_2'}{k_0} + \frac{v_1}{\omega|\sin\Omega|}\right)^2 \tag{36}$$

$$\langle\Delta x\Delta y\rangle = -\frac{1}{d_{22}k_0^2}\left(\frac{r_2'}{k_0} + \frac{v_1}{\omega|\sin\Omega|}\right)\left(r_1' - r_3'\cot\Omega - \frac{a_1}{\omega^2\sin^2\Omega}\right) \tag{37}$$

$$\langle(\Delta y)^2\rangle = d_{22} + \frac{1}{k_0^2}\left(\frac{1}{d_{22}}\left(r_1' - r_3'\cot\Omega - \frac{a_1}{\omega^2\sin^2\Omega}\right)^2 + \frac{1}{d_{11}}\left(\frac{r_2'}{k_0} + \frac{v_1}{\omega|\sin\Omega|}\right)^2\right) \tag{38}$$

These results furnish us with a quantitative measure of the defocusing associated with incorrect motion compensation; in particular we note the results which describe defocussing due to Fourier component sampling on a conical surface are not supplemented additively but in a more subtle fashion,e.g.

$$\langle(\Delta x)^2\rangle \neq d_{11} + \frac{r_2'^2}{d_{22}k_0^2} + \frac{v_1^2}{d_{22}k_0^2\omega^2\sin^2\Omega}$$

The extension of standard ISAR theory to include these effects would be difficult, both conceptually and in terms of its algebraic complexity.

3 Simulation Results

In this section we describe computer simulations which verify the theoretical results discussed in the previous section. Simulated images of a ship model illustrate how different target rotations generate images projected onto different planes. The variation of the phase of the point spread function is analysed in detail, allowing us to describe the interference effects in images of closely spaced scatterers observed in simulated ship images. Finally we demonstrate the effects of errors in motion compensation on the amplitude and phase of the point spread function and the more pronounced interference effects observed in defocused images. Throughout the agreement we obtain between theory and simulation is excellent and provides a very satisfactory confirmation of our formal analysis.

3.1 Simulation Methods

The simulation procedure we adopt consists of two stages: the generation of a succession of target/platform configurations and the evaluation of the monostatic returns

in each of these configurations for a range of transmitted frequencies, and their subsequent processing to yield a simulated ISAR image. As the successive steps in the imaging process are mirrored very closely in our formal development we will, where appropriate, employ a notation based on that of the previous section. Throughout we assume that the radar platform is stationary (i.e that $r(t) = r$); referred to our standard coordinate system it has a position vector $\mathbf{r} = (r, 0, 0)$. The target consists in general of a set of point scatterers, labeled by index m. To each point scatterer we assign an initial position $\delta\bar{\mathbf{r}} + \mathbf{r}'_{\mathbf{m}}$; its subsequent positions are generated by the straightforward numerical implementation of (2),(30) i.e. at time $t_l = l\Delta t$ the position of the m^{th} scatterer is given by

$$(\delta\bar{\mathbf{r}} + \mathbf{v}t_l + \frac{1}{2}\mathbf{a}t_l^2) + \mathbf{M}_s(t_l).\mathbf{r}'_m$$

$\mathbf{M}_s(t_l)$ generates the target rotation through

$$\mathbf{M}_s(t_l).\mathbf{r}'_m = (1 - \cos(\omega t_l))\mathbf{n}_s(\mathbf{n}_s.\mathbf{r}'_m) + \cos(\omega t_l)\mathbf{r}'_m + \sin(\omega t_l)\mathbf{n}_s \wedge \mathbf{r}'_m. \qquad (39)$$

At each time t_l a set of motion compensated returns is calculated as

$$S_{2,m}(k_j, t_l) = \exp(-ik_j r)\exp(ik_j|\mathbf{r} - \delta\mathbf{r}(t_l) - \mathbf{M}_s(t_l).\mathbf{r}'_m|) \qquad (40)$$

the wavenumber k_j being given by

$$k_j = k_0 + \frac{4\pi j\Delta f}{c}$$

where Δf is the frequency modulation increment. By stepping through equal numbers of positive and negative integer values of j, l and summing over all the point scatterers in the target a 256×256 array of backscattered returns is built up. This is then weighted with a Gaussian function centered on $j = l = 0$, corresponding to the weighting function $\tilde{H}(\mathbf{k}_H)$. To simulate the imaging process we employ a two dimensional Fast Fourier transform to effect the inversion of this weighted array. The equivalence of this procedure to standard ISAR processing [4] is discussed in [1]; this relationship is represented schematically in Figure 1. The frequency modulation, experimental geometry and target rotation rate define the length scales characteristic of the image, the 1 coordinate being discretised in units of

$$\text{xstep} = \frac{c}{512\Delta f}$$

and the 2 coordinate in units of

$$\text{ystep} = \frac{c}{512\Delta t f_0 \omega_s |\sin\Omega|}$$

(In comparing simulation and theoretical results care must be taken to ensure that distances within the image plane are always scaled appropriately in these units and that the convention $\mathbf{n} = -\mathbf{n}_s$ is observed throughout.)

3.2 Ship Images

Our first set of simulation results illustrates the way in which different target rotational motions or, more specifically, the axes about which these rotations occur, generate ISAR images projected onto different planes. The axis of image projection can be thought of as that axis along which we have no information about position. We recall that the range profile provides us with information along $\mathbf{r}$, while the Doppler profile provides us with information along $(\mathbf{n}_s \wedge \mathbf{r})$. Consequently the axis of projection must be normal to both these vectors and so lies along $\mathbf{r} \wedge (\mathbf{n}_s \wedge \mathbf{r})$ i.e. the image is always formed in the $(1,2)$ plane of our standard coordinate system. We have simulated images of a 250 scatterer model of an F88 frigate undergoing different rotational motions, which we present along with line drawings of the ship model, projected onto the $(1,2)$ planes defined by these motions. These are shown in Figures 3-6, where yaw, pitch and composite rotations can be seen to produce plan, side, 45° elevated side, and three quarters views of the ship . Table 1 summarises the radar parameters and ship motions used to produce each image, allowing a comparison between their theoretical and actual planes of projection. Visual inspection reveals that these planes are indeed coincident.

3.3 Phase Effects

A more exacting, quantitative test of our theory is provided by the comparison of our point spread function results (21–23) with the simulated images of a single point scatterer. In our earlier work [1] we demonstrated the satisfactory agreement obtained between theory and simulation for the amplitude variation within the image of a single point. We now demonstrate that the phase variation within such images is also well described by these results. In Figures 8,9 we present a comparison of the variation in phase in simulated images obtained as described in Table 2 and our corresponding theoretical predictions. (Throughout this report we present our results in a colour-coded contour plot format. Amplitude will be displayed in arbitrary units (which will, of course, be the same in comparing any particular set of simulated and theoretical results) while phase will be presented in radians and be taken to lie in the range $[-\pi, +\pi]$. We also draw the reader's attention to the fact that, in Table 2, scatterer position vectors are presented in Cartesian component form; all other vectors are presented the (r, θ, ϕ) spherical polar form illustrated in Figure 2.) The agreement can be seen to be very satisfactory. It should be stressed that, in obtaining these results, care was taken to ensure that the simulations were carried out in the far field limit, i.e. that (if $r'_\perp$ is the component of the target's position vector perpendicular to the line of sight vector (1,0,0)) the Fraunhofer criterion [5]

$$\frac{k_0 r'^2_\perp}{r} \ll 1 \tag{41}$$

was satisfied.

In the course of our ship image simulations it was noticed that when a target contained several point scatterers placed in close proximity the image obtained frequently showed features most readily interpreted as interference effects. We now present results analysing this phenomenon in more detail. If we have more than one scatterer in the target we will obtain an image given by the coherent sum of the complex point spread functions (21) centred on the positions of these point scatterers, which can in general display interference effects manifested as intensity maxima and minima. Thus the form of the complex image of a set of scatterers, labelled by index m, is given by

$$f(\mathbf{r}_H)' = \sum_m H(\mathbf{r}_H, \mathbf{r}'_m) \tag{42}$$

where (c.f. (21)) each of the $H(\mathbf{r}_H, \mathbf{r}'_m)$ depends on the position vector $\mathbf{r}'_m$ of the associated point scatterer. The complicated dependence of the phase and amplitude of the resulting complex image on the target and experimental geometry can lead to quite subtle features appearing in the imagery, differing from those expected from a superposition of the intensities of the signatures of the individual point scatterers. This effect is illustrated in Figure 10. Figure 10a shows the intensity image of a point scatterer at (0,100,0) relative to the centre of mass of the target, rotating about an axis along the 3-axis while Figure 10b shows the simulated intensity image of two points at (0,100,0) and (0,101,0). Figure 10c show the results obtained by adding the intensities of images of points at (0,100,0) and (0,101,0) incoherently. This does not agree with the simulation. However the theoretical result (Figure 10d) based on Equation (42) is found to be in close agreement with the simulation. It was also noted that the simulated interference pattern becomes asymmetric when the radar is taken out of the far-field limit i.e. when the inequality (41) was not satisfied. These near-field effects, resulting from the curvature of the wave front incident on the target, have recently been analysed in considerable detail and are discussed elsewhere [6].

Finally Figures 11 and 12 show the excellent agreement between simulation and theory for ten closely spaced scatterers. Figures 11a and 11b illustrate the agreement between the amplitude variation whilst Figures 12a and 12b show the phase variation. Taken as a whole the results we have presented so far provide adequate confimation of the validity of our description of the point spread function of an ISAR system for which motion compensation is perfect.

3.4 Effects of Incorrect Motion Compensation

Our final set of simulation results illustrates and confirms our analysis of the effects of incorrect motion compensation. Figure 13 shows the amplitude distribution of the image of a non-rotating point target with an uncompensated velocity and acceleration. Once again colour-coded contour plots of the simulated images are presented, along with plots of the appropriate theoretical results. The corresponding phase plots are shown in Figure 14. These results can be compared with those presented in Figures 15 and 16, which show the amplitude and phase plots for the image of a rotating point target with the same uncompensated velocity and acceleration. The excellent agreement between theory and simulation is evident both visually and in the numerical results given in Table 3 for $\langle \Delta x^2 \rangle$, $\langle \Delta y^2 \rangle$, and $\langle \Delta x \Delta y \rangle$. The differences between Figures 13,14 and 15,16 illustrate the effect of the coupling between 'conical polar formatting' and centre of mass motion effects manifest in the results (36–38).

Figure 17a shows the amplitude distribution plot for the image of two closely spaced point targets assuming perfect motion compensation. Theory (17b) and simulation are presented and can be seen to be in agreement. The corresponding plots for the image of equivalent point targets rotating in a coordinate system with an uncompensated velocity and acceleration are shown in Figure 17c/d. The effects of centre of mass motion in defocussing the image and introducing discernible interference features are evident in the simulated results, which can be seen to be described accurately by the theory. Table 2 shows the parameters used in these simulations.

4 Autofocusing

The ultimate objective of this work is to establish a capabilty to make better use of radar data for target localisation and identification. It is therefore desirable to derive well focused images in situations where motion parameters are only known approximately. One approach to this is to estimate the unknown motions by maximising the focusing of the image with respect to each of the unknowns. Thus for SAR the across-track acceleration is often estimated by maximising the image contrast or minimsing the sub-aperture spatial offset. For more complicated problems, such as imaging a moving and rotating ship from an airborne sideways looking radar, the unknown parameter space has too many dimensions and subtle defocusing interactions between motions, to allow a practical image optimisation.

The analysis presented in earlier sections of this report and [1] shows that the defocusing of SAR, ISAR and hybrid SAR/ISAR images can be expressed concisely in a matrix form. Manipulation of the results show how the following effects cause

image distortion and defocusing,

(a) Approximations in the processing, e.g. 'Range-Doppler processing',

(b) Unwanted motions, e.g. rotational accelerations,

(c) Errors in estimations of other motion parameters, e.g. target rotation rate, target and radar velocities and accelerations, and

(d) Scatterers on the target offset from the imaging plane.

A particular strength of the approach is the grouping together of terms which cause similar effects on imagery, and are therefore ambiguous to interpretation. Simple examples of this are

(a) Rotation rate and image scaling in ISAR, and

(b) The first order effect of line-of-sight motion and azimuthal position in SAR imagery.

The formalism therefore allows the search for autofocusing to be undertaken within the correct unambiguous parameter space. Also, specific functional relationships, between the degree of defocusing and the position on the target, are associated with each type of motion. This suggests that some decoupling of searches of sets of parameters may be possible. Finally the quantitative linkage between defocusing and actual motion should provide bounds within which to undertake the searches, and measures of the accuracy of the focus achieved.

Specific algorithms have not yet been proposed, nor have focus optimisation measures been tested. One particular concern relates to the use of contrast maximisation, since one finding of this work has been the large phase variations associated with defocused point spread functions. This may result in high contrast fringes between large defocused scatterers of the type we have analysed in section 3.4. Future work will address these features, with the aim of developing a well founded SAR/ISAR autofocusing method, which performs better than the current *ad-hoc* approaches and provides a higher yield of classifiable target images.

5 Conclusions

In this Memorandum we have discussed many features of far field ISAR images in much greater detail than has been done previously. This has been made possible by the application of the general theory of synthetic aperture imaging introduced in our earlier work [1]. Our present work has confirmed the utility and power of this method and at the same time has simplified and clarified many of the calculational procedures involved in its application to specific problems. Extensive computer simulations have confirmed its value in the analysis of the phase characteristics of the point spread function and the occurence of interference effects in synthetic aperture images of closely spaced scatterers. An essentially complete description of the effects of errors in motion compensation in far-field ISAR imaging has also been achieved, and has again been verified by computer simulation. These developments have furnished a very sound foundation for subsequent work in which ISAR images will be enhanced by autofocus methods. Consequently we have presented a preliminary assessment of the difficulties likely to be encountered in implementing these techniques and their evident amelioration by the results of our work to date.

References

1. Tough, R.J.A. and Ward, K.D., A theory for hybrid SAR/ISAR radar imaging, RSRE Memorandum 4532 (1991).

2. Tough, R.J.A., The coordinate-free representation of Rotational Motions, RSRE Memorandum 4445 (1991)

3. Kibble, T.W.B., Classical Mechanics, Chap 5, McGraw Hill, New York (1966)

4. Wehner, D.R., High Resolution Radar, Chap 5, Artech House, Norwood MA, (1987)

5. Hecht, E., Optics, Chap 10, Addison-Wesley, Reading, MA., (1987)

6. Tough, R.J.A. and Porter, N.J., ISAR imaging of maritime targets in the near field DRA Memorandum 4680 (1992)

Table Of Figures

Table 1 - Parameters for ship images

Figure No	Line of Sight **k**	Rotation axis **n**	Theoretical Axis $-\mathbf{k} \wedge (\mathbf{n} \wedge \mathbf{k})$	Actual Axis of Projection
3	(1,0,0)	(0,0,1)	(0,0,-1)	(0,0,-1)
4	(1,0,0)	(0,1,0)	(0,-1,0)	(0,-1,0)
5	(1,0,0)	(1,1,1)	(0,-1,-1)	(0,-1,-1)
6	(1,-1,0)	(1,1,1)	(-1,-1,-1)	(-1,-1,-1)

Rate of rotation 4 degs/sec.

Centre frequency f_o = 10GHz.

Step frequency Δf = 1 MHz.

Time Step Δt= 1.8ms.

S.d. of Gaussian Weighting 25

Motion compensation No velocity or acceleration correction.

Radar positioned at far field limit.

Table 2 - Parameters for Figures

Figure No	Rotation axis **n**	Displacement Δ**r**	Velocity **v**	Acceleration **a**	Position r'
8	(1,0,0)	(0,0,0)	(0,0,0)	(0,0,0)	(67,67,0)
9a	(1,45,0)	(0,0,0)	(0,0,0)	(0,0,0)	(67,67,67)
9b	(1,60,0)	(0,0,0)	(0,0,0)	(0,0,0)	(134,67,134)
11	(1,0,0)	(0,0,0)	(0,0,0)	(0,0,0)	(49,49,49) (50,52,48) (53,50,50) (51,51,0) (50,48,0) (47,47,52) (52,48,30) (50,50,30) (47,53,50) (50,50,50)
13a 15a	(1,45,0) (1,45,0)	(1,34,50) (1,34,50)	(1,57,63) (1,57,63)	(1,30,33) (1,30,33)	(0,0,0) (67,67,0)
13c 15c	(1,45,0) (1,45,0)	(1,64,30) (1,64,30)	(4,214,63) (4,214,63)	(2,70,60) (2,70,60)	(0,0,0) (67,67,0)
17a 17c	(1,0,0) (1,0,0)	(0,0,0) (0,0,0)	(0,0,0) (2,60,60)	(0,0,0) (3,50,40)	(16,15,0) (16,17,0) (16,15,0) (16,17,0)

Rate of rotation 4 degs/sec.

Coordinate Systems Position vector in (x, y, z), others in (r, θ, ϕ)

Centre frequency f_o = 10GHz.

Step frequency Δf = 3 MHz.

Time Step Δt= 5ms.

S.d. of Gaussian Weighting 25

Motion compensation No velocity or acceleration correction.

Radar positioned at far field limit.

Table 3 - Moments comparing theory and simulation

	(0,0,0)				(67,67,0)			
	Figure13a		Figure13c		Figure15a		Figure15c	
	Sim.	Theory	Sim.	Theory	Sim.	Theory	Sim.	Theory
$\langle x^2 \rangle$	0.103	0.103	0.117	0.117	0.235	0.235	0.393	0.393
$\langle y^2 \rangle$	1.509	1.511	5.824	5.835	0.916	0.913	4.426	4.446
$\langle xy \rangle$	-0.055	-0.055	0.302	0.302	0.272	0.275	1.058	1.062

Simulation Results - derived numerically from image.

Theoretical Results - derived from equations [44-46].

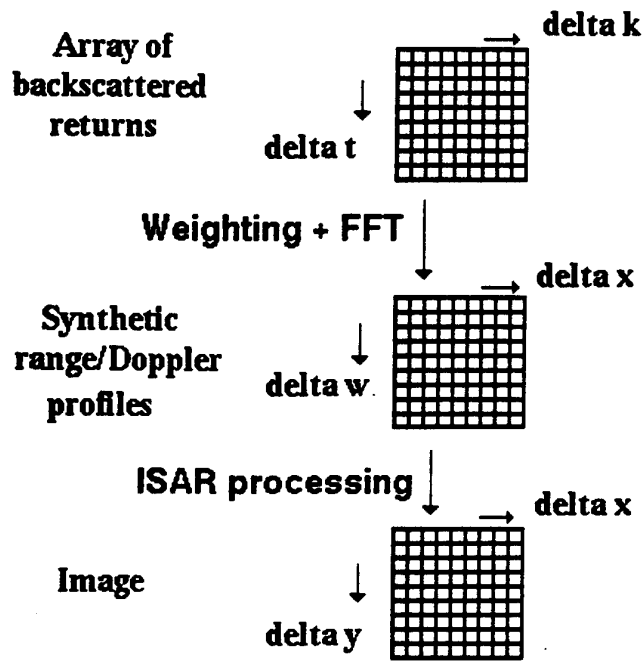

Figure 1 A diagrammatic summary of the simulated imaging process.

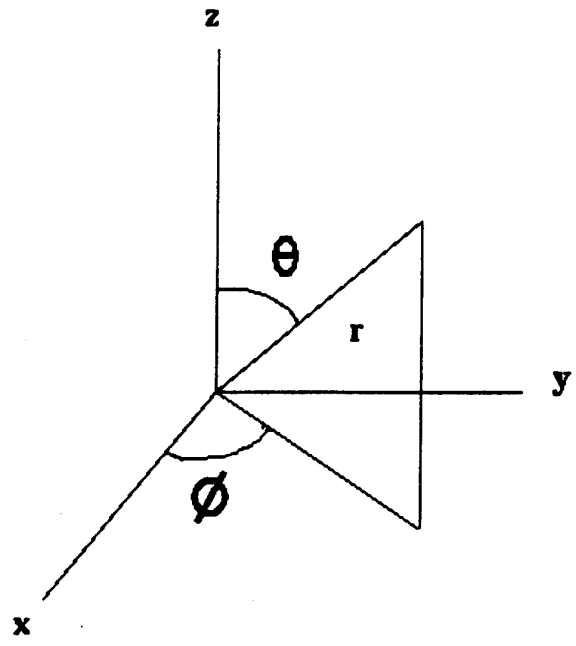

Figure 2 The rotational coordinate system used in the theory and the simulations.

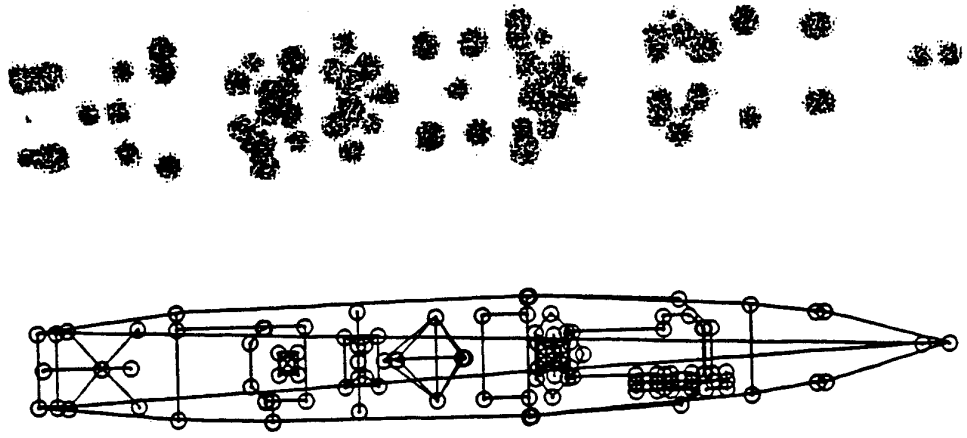

Figure 3 A simulated image of a point scatterer modelled ship in comparison with a plan view of the ship. In this case the ship is yawing at a rate of $4°/sec.$

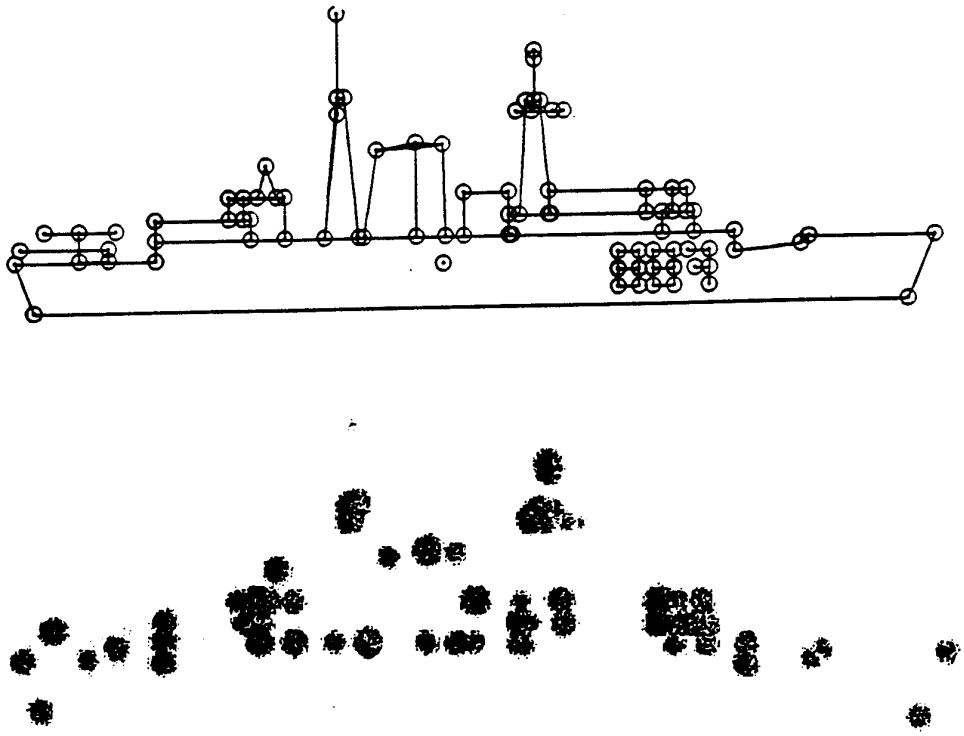

Figure 4 A simulated image of a point scatterer modelled ship in comparison with a side view of the ship. In this case the ship is pitching at a rate of $4°/sec.$

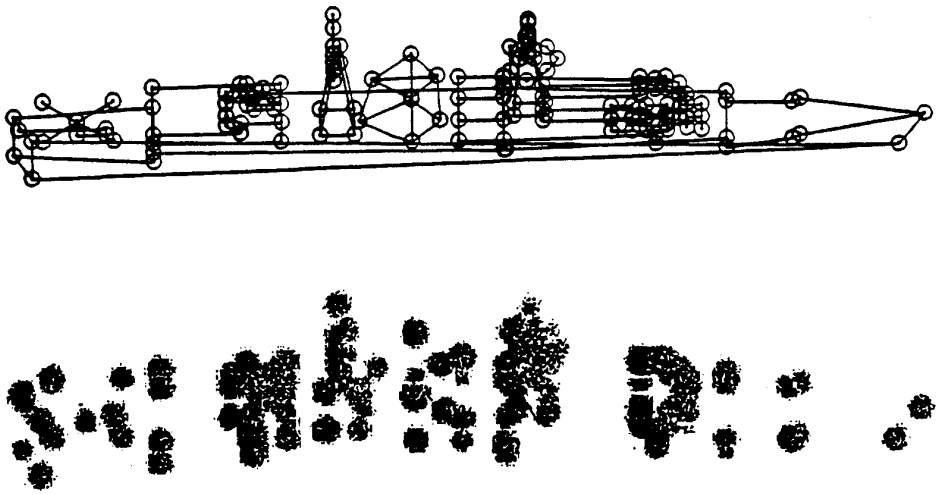

Figure 5 A simulated image of a point scatterer modelled ship in comparison with a 45° elevated side view of the ship. The ship is observed along the x-axis and its motion combines yaw, pitch, and roll,

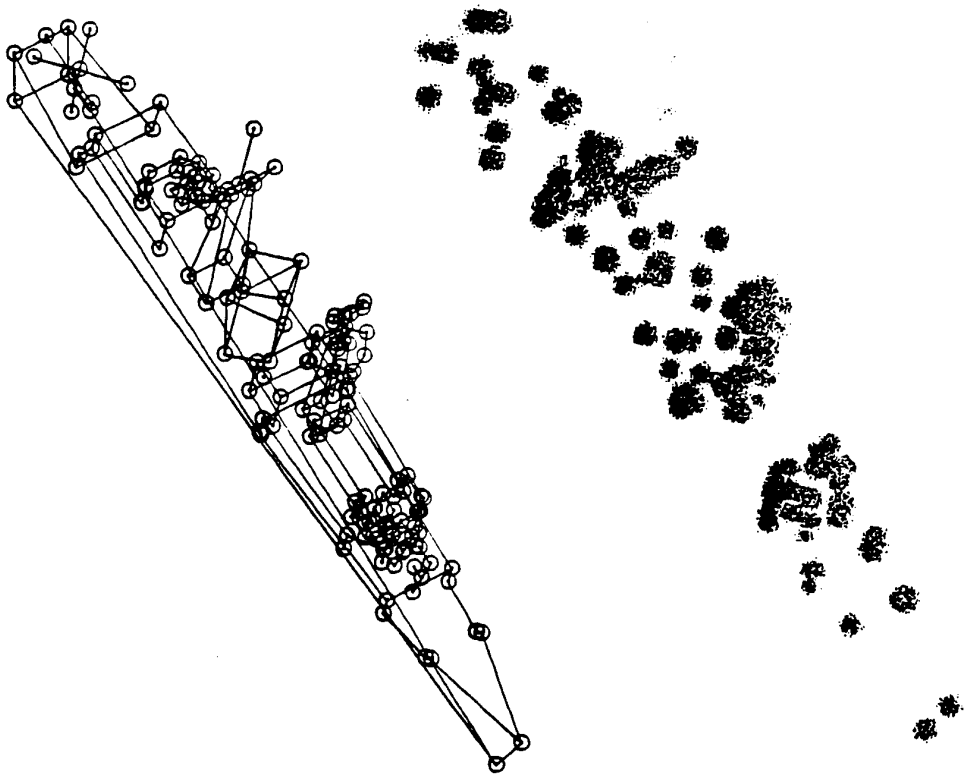

Figure 6 A simulated image of a point scatterer modelled ship in comparison with a three-quarters view of the ship. The ship is observed along the $-xy$-axis and its motion combines yaw, pitch, and roll.

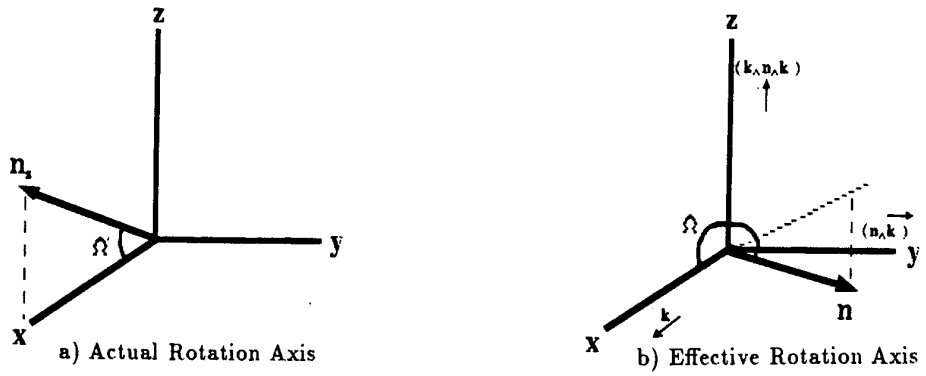

Figure 7 Rotation axis of simulation

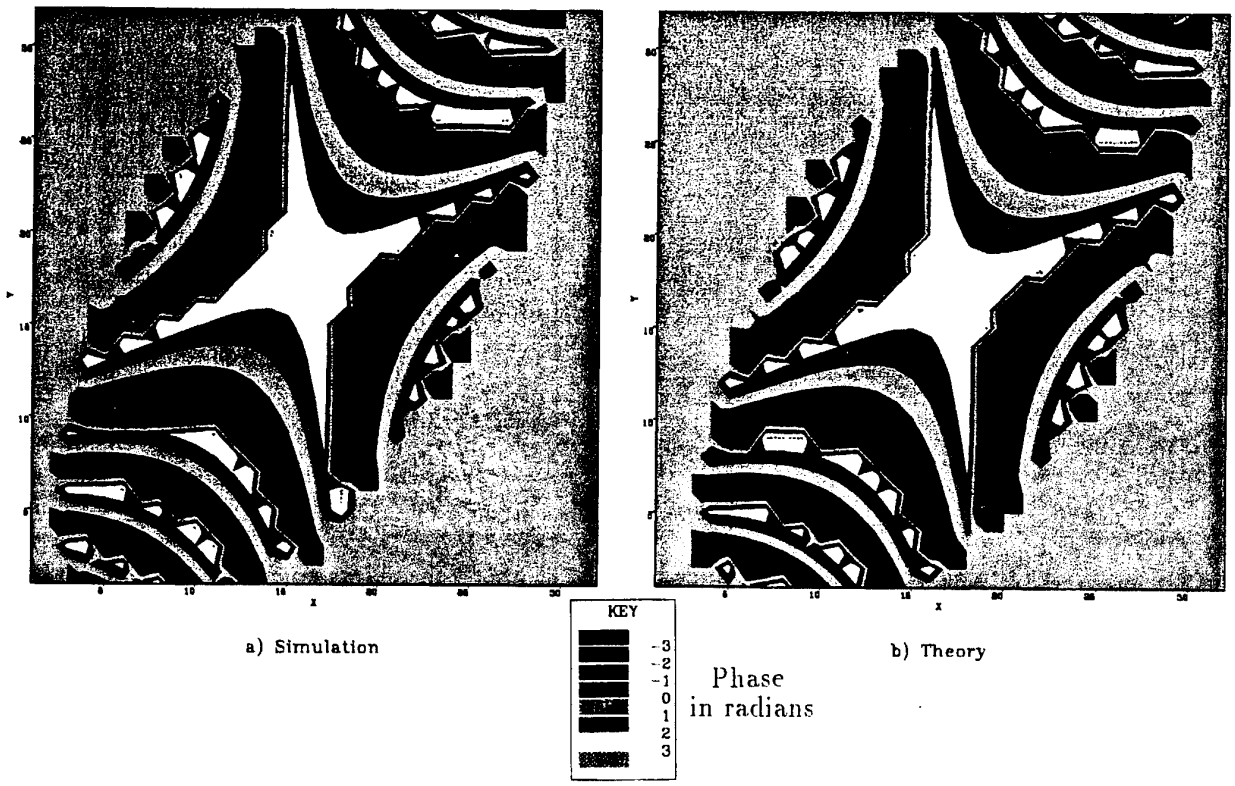

Figure 8 Phase plot of image of scatterer at (67,67,0)

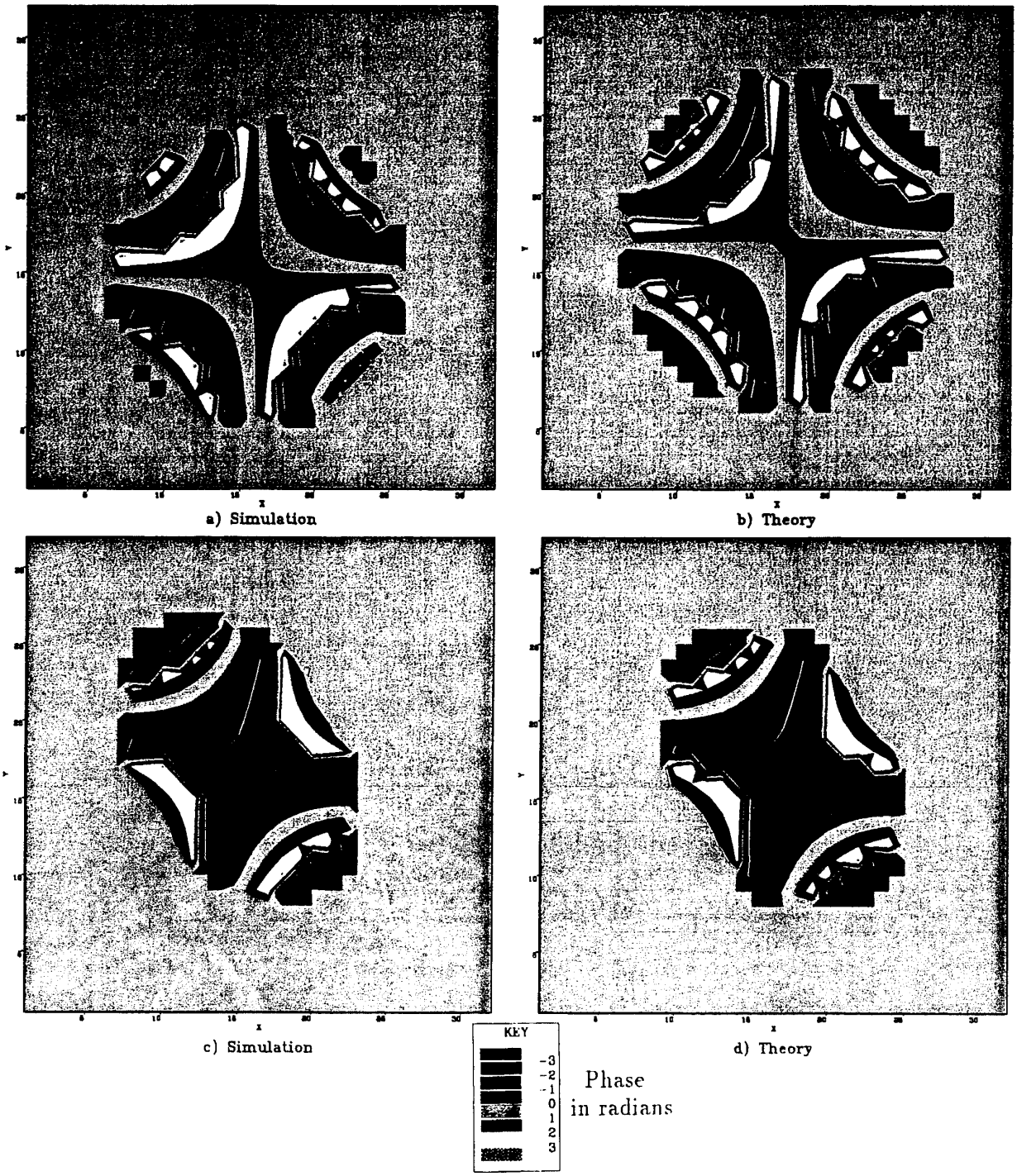

Figure 9 Simulated and theoretical images for two point scatterers
(a),(b) Point at (67,67,0),n=(4,0,45). (c),(d) Point at (134,67,134),n=(4,0,60)

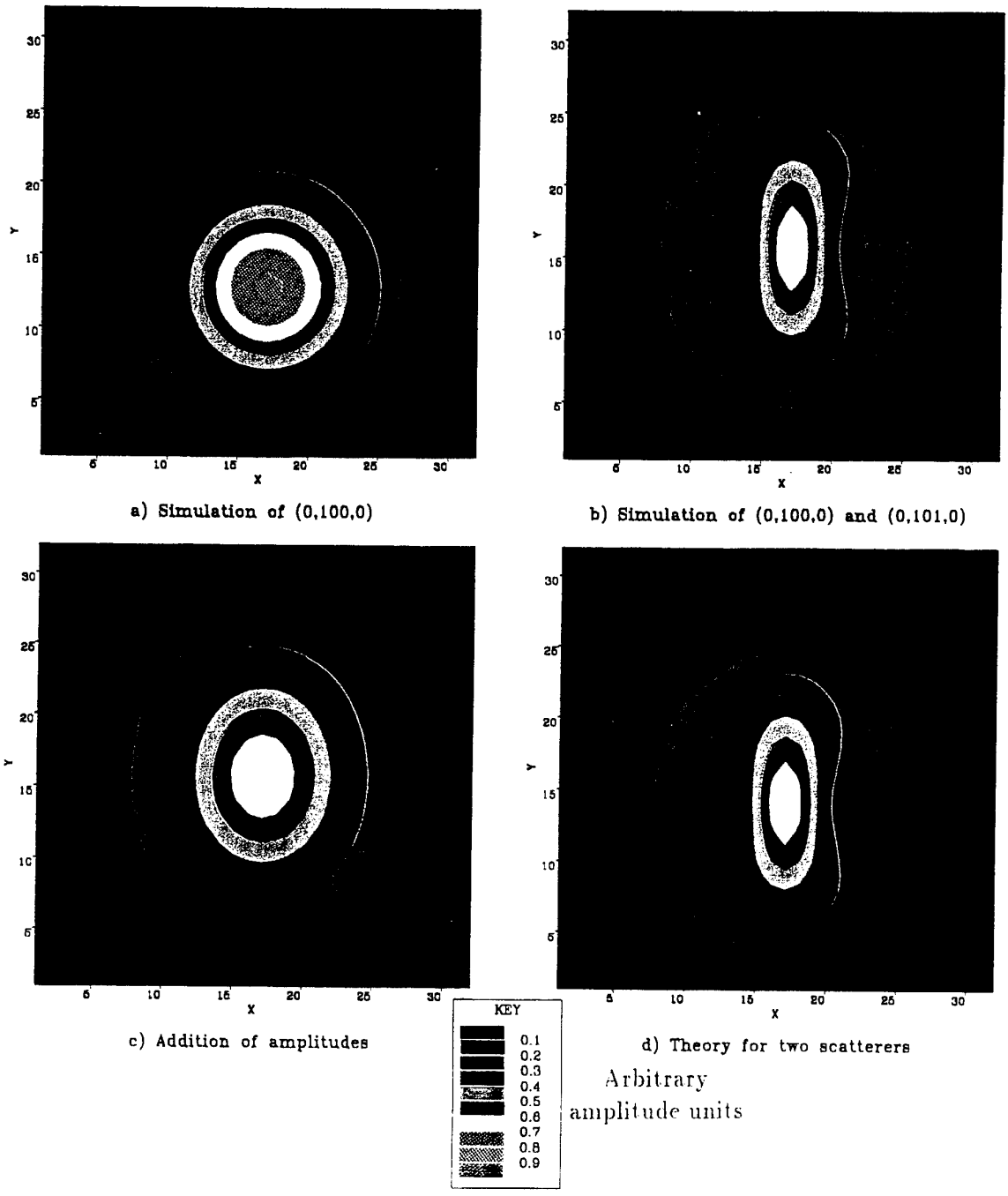

Figure 10 The effects of coherent and incoherent addition of scatterers, and comparison with simulation.

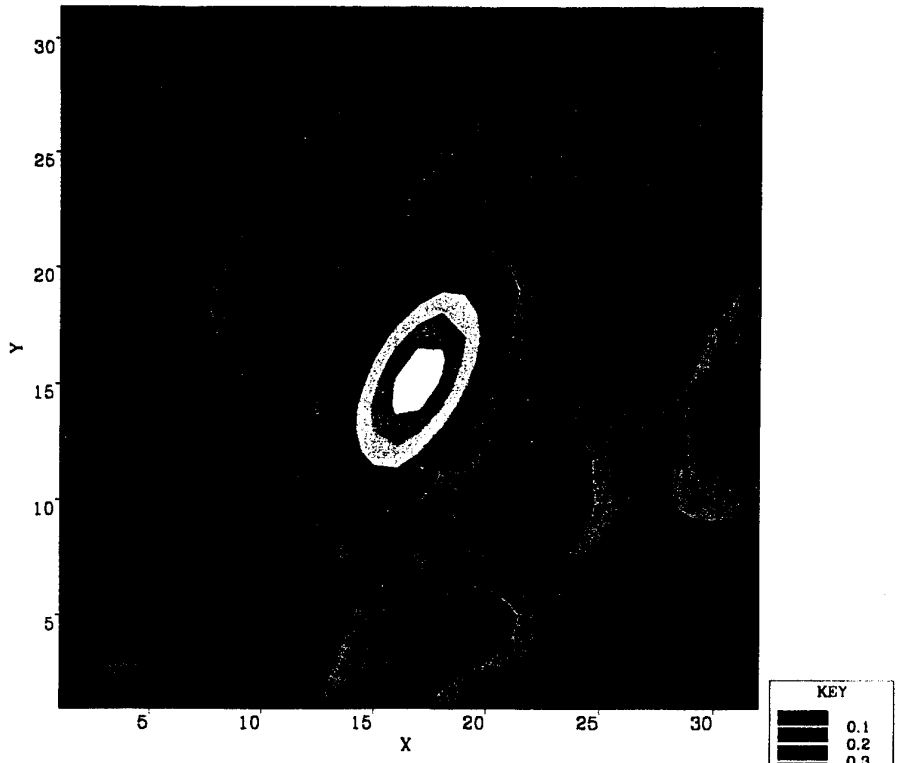

a) Simulation

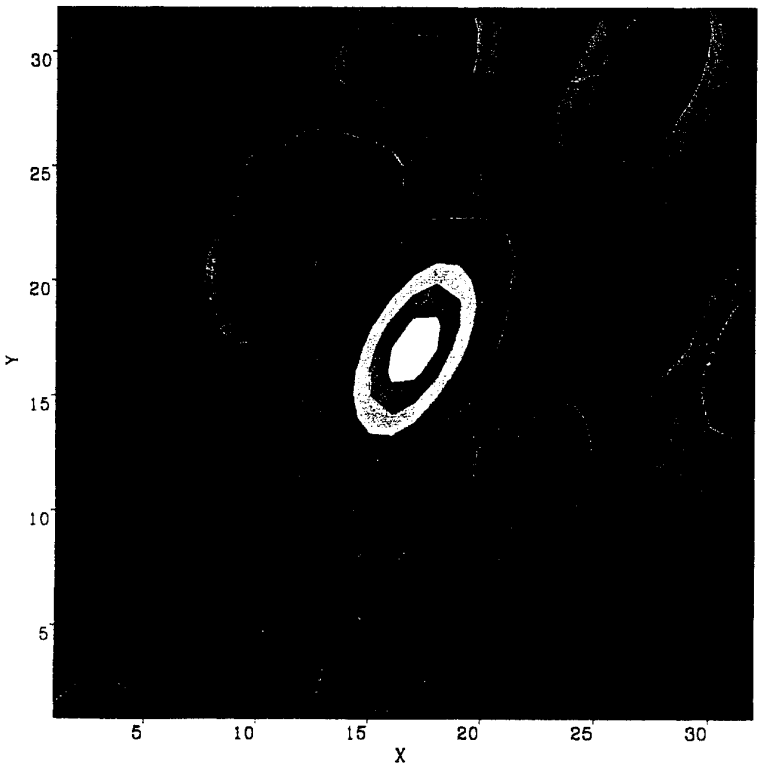

b) Theory

Figure 11 Amplitude plot showing the interference between 10 scatterers. Details in Table 2.

a) Simulation

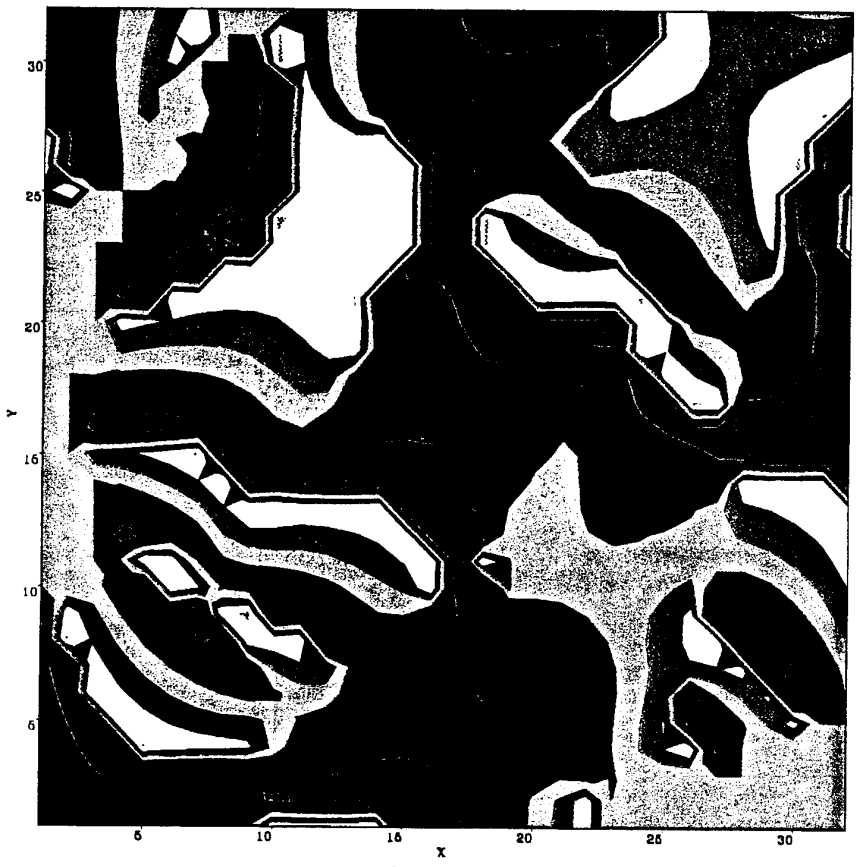

b) Theory

Figure 12 Phase plot showing the interference between 10 scatterers. Details in Table 2.

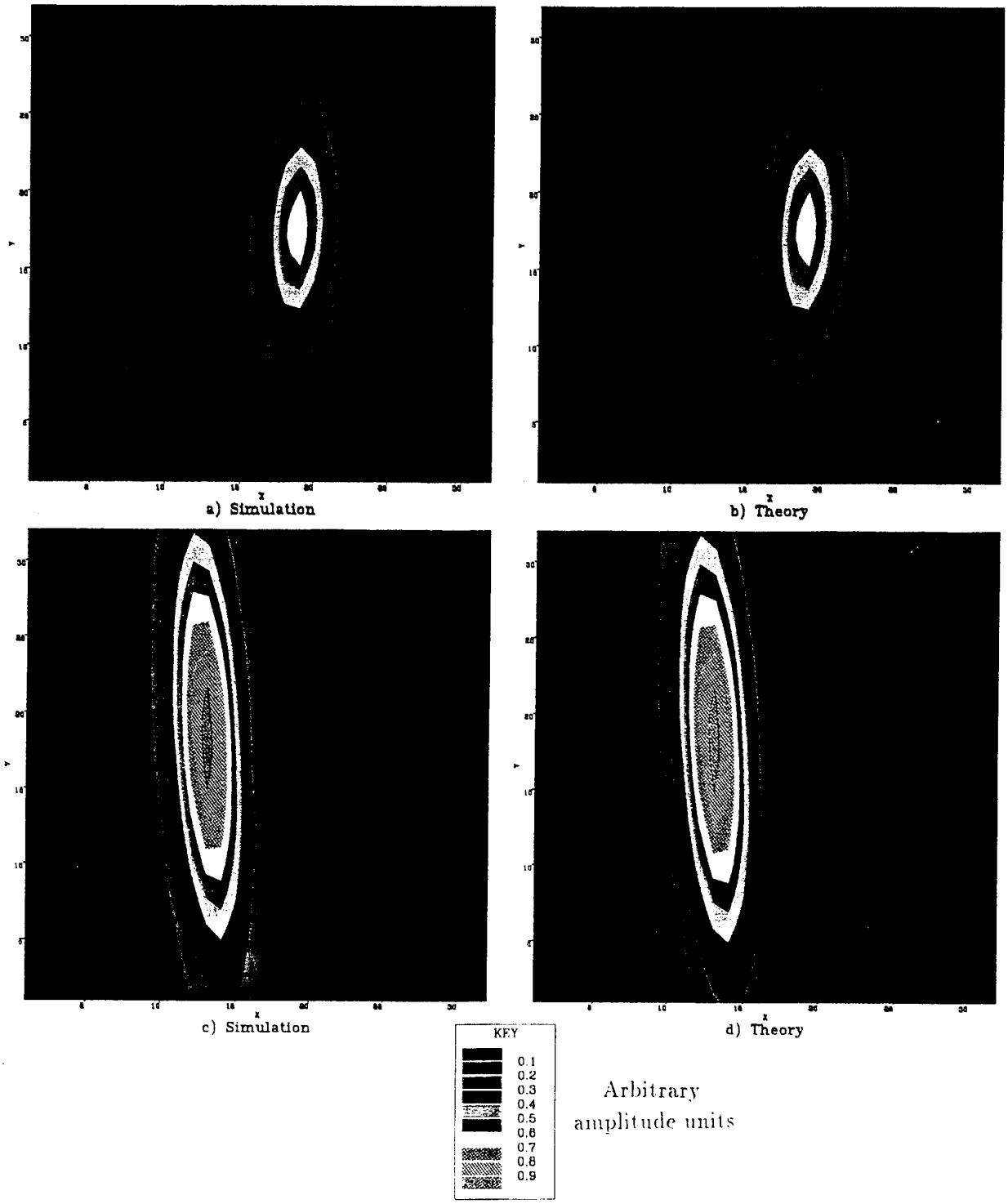

Figure 13 Amplitude plot showing the effect of two centre of mass motions on a scatterer at (0,0,0).

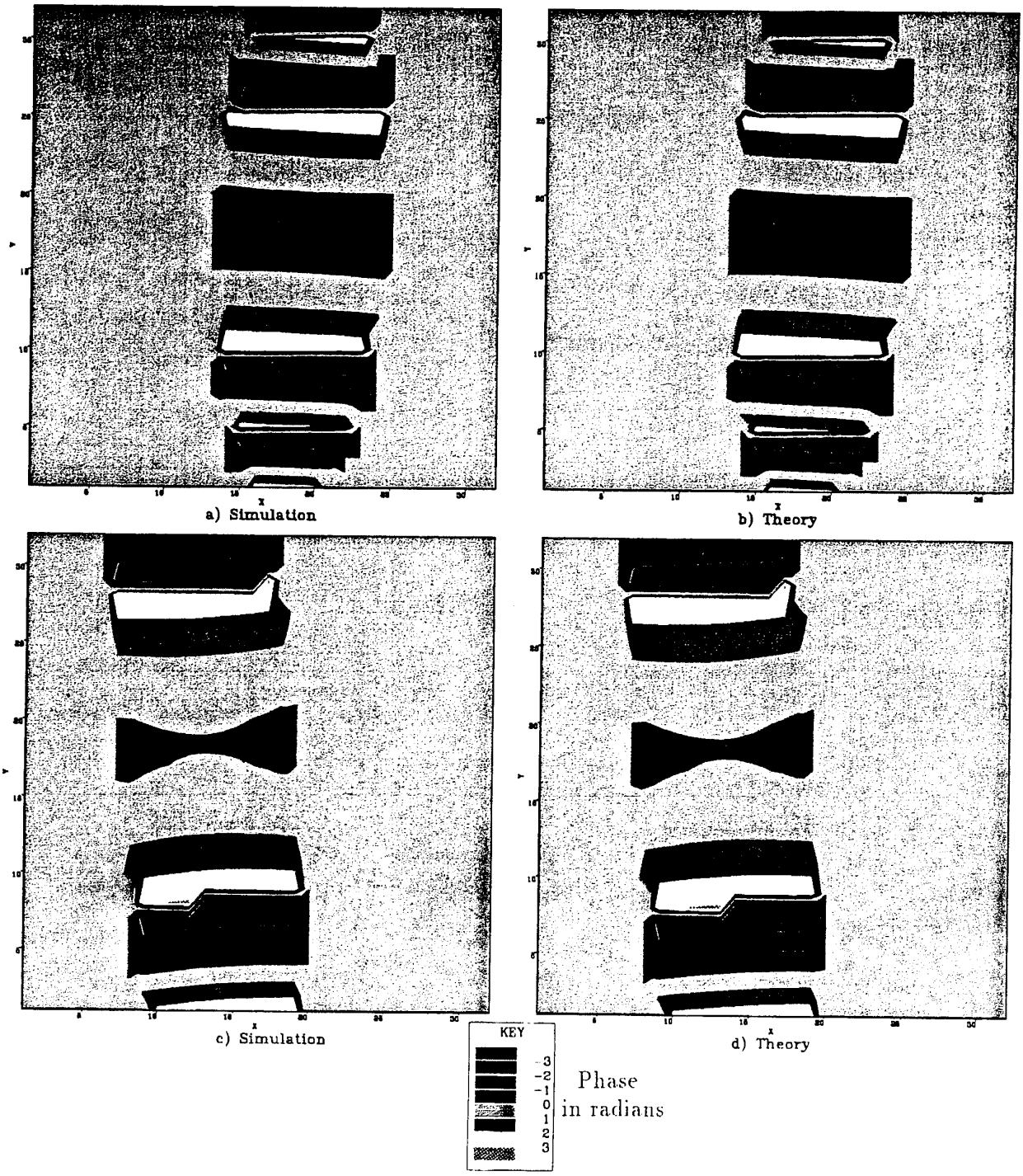

Figure 14 Phase plot showing the effect of two centre of mass motions on a scatterer at (0,0,0).

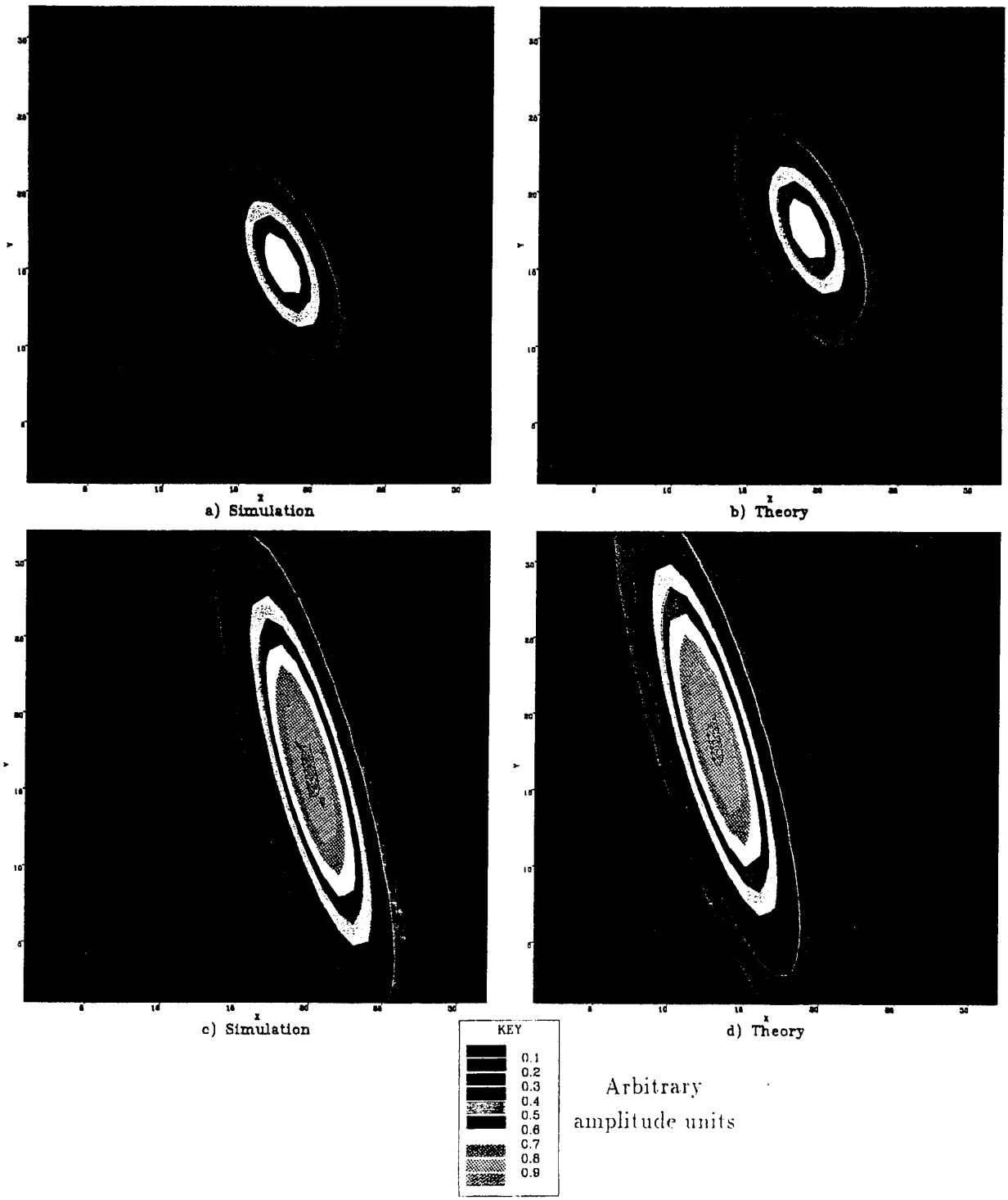

Figure 15 Amplitude plot showing the effect of two different centre of mass motions on a scatterer at (67,67,0) – same motions as Figure 13.

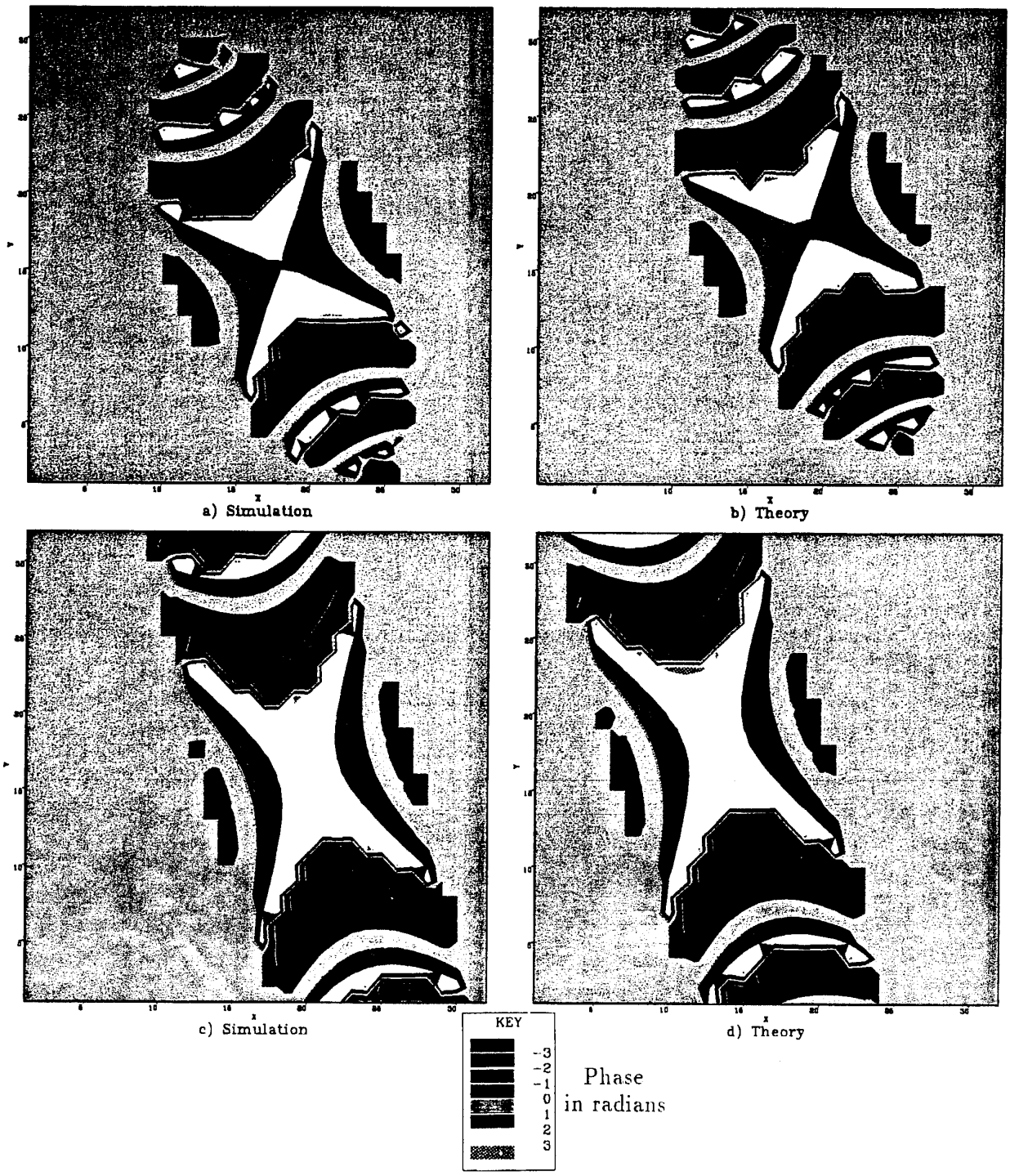

Figure 16 Phase plot showing the effect of two different centre of mass motions on a scatterer at (67,67,0) – same motions as Figure 14.

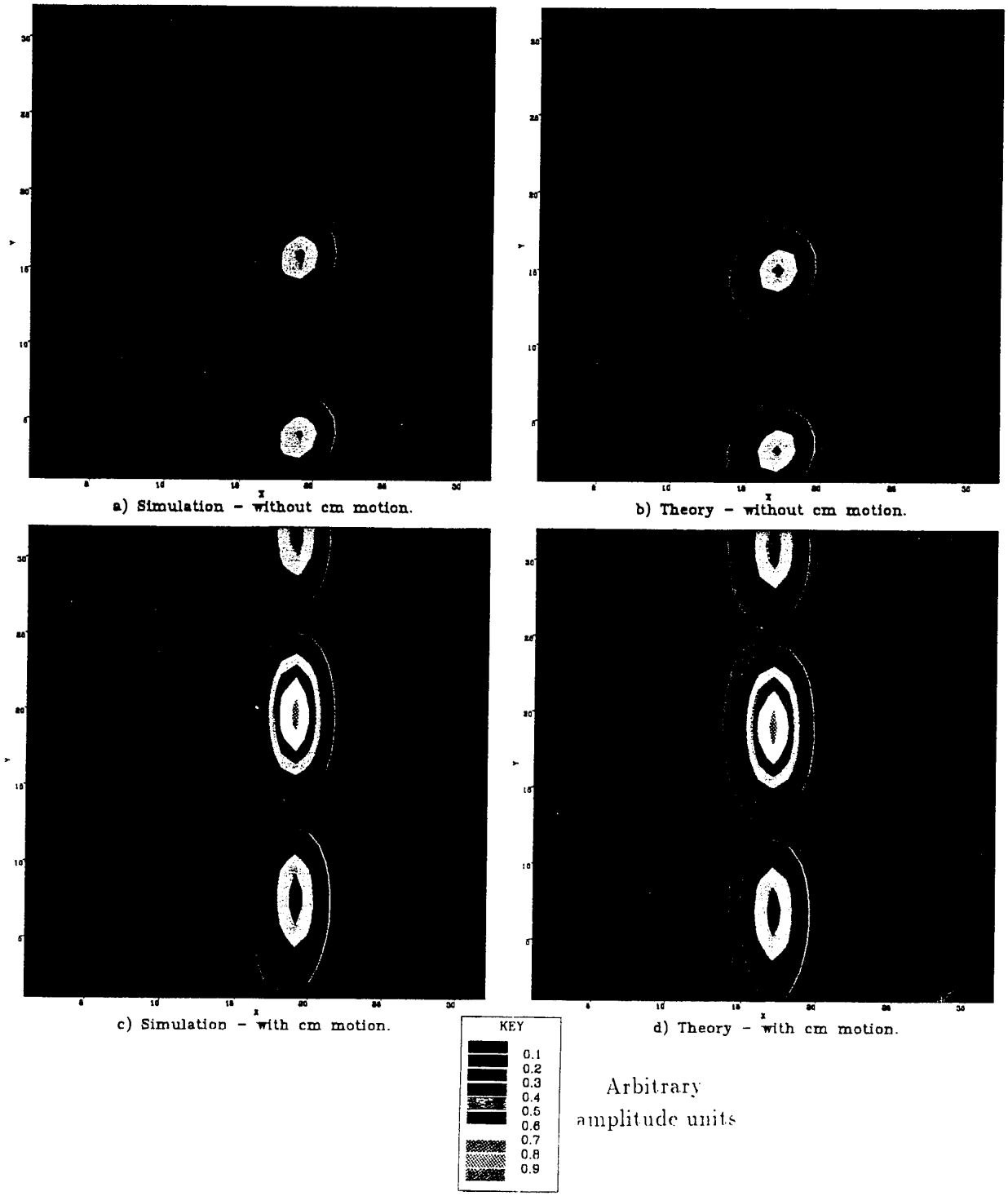

Figure 17 Interference between two scatterers (16.15.0) and (16.17.0), with and without a centre of mass motion of the target.

REPORT DOCUMENTATION PAGE

DRIC Reference Number (If known) .....

Overall security classification of sheet ..... UNCLASSIFIED .....

(As far as possible this sheet should contain only unclassified information. If it is necessary to enter classified information, the field concerned must be marked to indicate the classification, eg (R), (C) or (S).

Originators Reference/Report No.	Month	Year
MEMO 4577	SEPTEMBER	1992

Originators Name and Location
DRA, ST ANDREWS ROAD
MALVERN, WORCS WR14 3PS

Monitoring Agency Name and Location

Title

ISAR IMAGING OF MARITIME TARGETS:
THEORY AND SIMULATION

Report Security Classification	Title Classification (U, R, C or S)
UNCLASSIFIED	U

Foreign Language Title (in the case of translations)

Conference Details

Agency Reference	Contract Number and Period

Project Number	Other References

Authors	Pagination and Ref
PORTER, N J; TOUGH, R J A; WARD, K D	34

Abstract

The theoretical analysis of synthetic aperture techniques presented in Memorandum 4532 is applied to the inverse synthetic aperture radar (ISAR) imaging of ship targets. The point spread function of an ISAR system is derived and discussed in detail. The explicit representation of phase information within our formalism makes possible the first thorough analysis of interference effects in synthetic aperture images of closely spaced scatterers. Effects of errors in motion compensation are also discussed in considerably greater depth than in earlier work. Computer simulation has provided us with a useful tool with which to verify our analytical results; we describe our simulation method and present a comprehensive selection of simulated images illustrating and confirming our theoretical analysis. Finally some practical implications of our results for the autofocusing of ISAR images are discussed.

This work was carried out under Defence Research Package AS02BM23.

Abstract Classification (U, R, C or S)
U

Descriptors

Distribution Statement (Enter any limitations on the distribution of the document)
UNLIMITED

S80/48